Journal of Materials Chemistry A

Accepted Manuscript

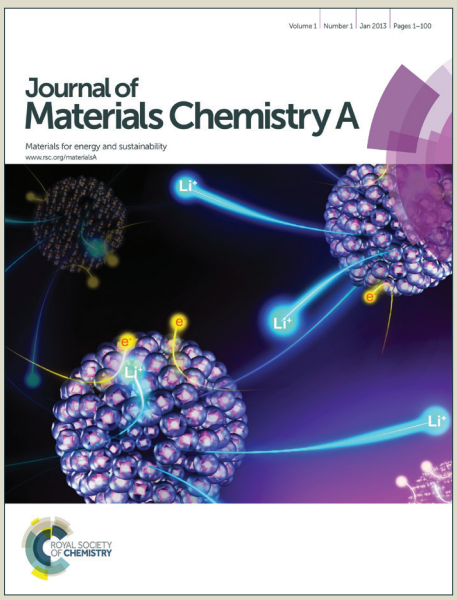

ROYAL SOCIETY OF CHEMISTRY

www.rsc.org/materialsA

Journals of Materials Chemistry A RSCPublishing

PAPER

Physical aging of polymers of intrinsic microporosity: a SAXS/WAXS study

Cite this: DOI: 10.1039/x0xx00000x

Amanda G. McDermott,[a†] Peter M. Budd,[b] Neil B. McKeown,[c‡] Coray M. Colina[a] and James Runt[a]

Received 29th April 2014,
Accepted 00th May 2014

DOI: 10.1039/x0xx00000x

www.rsc.org/MaterialsA

Porosity in polymers of intrinsic microporosity (PIMs) is closely related to free volume: it arises from a chain structure combining rigid segments with sites of contortion, producing a large concentration of interconnected pores smaller than 1 nm. Membranes of these polymers are subject to physical aging, which decreases their permeability and reduces their performance in gas separation. In this work, a robust interpretation of PIM X-ray scattering features is developed with support from molecular dynamics simulations. The sensitivity of scattering patterns to time, temperature and film thickness is shown to be qualitatively consistent with physical aging, demonstrating that these high-free-volume, porous polymeric glasses present a unique opportunity to study structural changes during physical aging using scattering methods. Quantitative modeling of PIM scattering patterns remains challenging, and the time resolution required to capture the initial aging stages of a single film is difficult to achieve with laboratory instruments. However, the spectrum of glassy states accessed by varying film thickness and aging temperature raises the possibility that there may be two distinct mechanisms of aging in PIMs.

Introduction

Highly permeable polymers show great promise for use as high-flux gas separation membranes[1]. However, physical aging, whereby initial free volume is lost and gas permeability is reduced, undermines their potential for commercial exploitation as membrane materials. To date, most studies of aging rely on the observation of the reduction in gas permeability rather than a direct structural analysis of the changes taking place within the polymer. Here we use X-ray scattering informed by molecular dynamics simulations to investigate physical aging in polymers of intrinsic microporosity (PIMs), an emerging class of highly permeable polymers[2].

PIMs are named in accord with the IUPAC nomenclature[3] defining 'microporous' materials as those featuring pores smaller than 2 nm. This convention has resulted in considerable disorganization in the literature: because materials with micron-sized pores are often termed 'microporous', true microporous materials are frequently lumped into a 'nanoporous' category (1 to 100 nm). However, the IUPAC categories of microporosity, mesoporosity and macroporosity demarcate significant differences in adsorption mechanisms that impact both performance in potential applications and the suitability of various characterization techniques[4]. In these true microporous materials, the size of pores is comparable to the size of small molecules that might diffuse through the bulk material or adsorb onto its interior surface. Such small molecules then interact with multiple pore walls simultaneously. This effect makes microporous materials effective both as adsorbents and as gas separation membranes: pore sizes can be tuned to discriminate based on molecule size, and the effect of energetic contributions is amplified by multi-wall interactions.

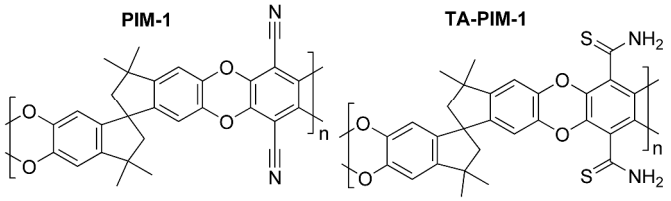

Figure 1. Chemical structures of PIM-1 and TA-PIM-1 (thioamide PIM-1).

PIMs employ a novel strategy to inhibit the efficient space-filling characteristic of polymers, combining rigid segments with sites of contortion (Figure 1). They feature high gas permeability[5] and are described as 'high free volume' polymers[6] although as discussed below, the quantitative relationship between porosity and free volume is poorly defined. Rather than consisting of a bulk phase with discrete pores, they are glassy materials with porosity consisting of

unoccupied volume that is well-connected, even from the perspective of a probe as large as a diffusing gas molecule.

PIMs' porosity is termed 'intrinsic' because they exhibit unusually high free volume and permeability regardless of processing conditions, although precise values of measured quantities are sensitive to sample history. PIM-1 is easily cast into a film from chloroform, and it exhibits no glass transition below its decomposition temperature of 370 °C.[7] BET analysis of powder adsorption isotherms using N_2 at 77 K has yielded surface areas ranging from 760 to 850 m^2/g.[5, 7]

Pore size distributions can be measured by techniques such as gas sorption isotherms and positron annihilation lifetime spectroscopy (PALS), but the results are sensitive to assumptions in the models used to interpret the data.[8, 9] Pore size distributions in PIM-1 vary in shape depending on whether they are measured by PALS or nitrogen adsorption or calculated from molecular dynamics simulations.[10-12] However, all agree that PIM-1 pore sizes are predominantly smaller than ~1 nm.

Like other glasses, PIM films physically age over time: their density increases, which means that their porosity and free volume also decrease. However, the property most dramatically affected by aging in PIMs is gas permeability, which has also been shown to decrease during aging in other glassy polymers[13]. Although permeability and density were not tracked during this experiment, a decrease in permeability due to aging has been measured in many studies of PIM-1[9, 14, 15] as well as PIM-1 composites.[16] Significant aging occurs even under ambient conditions, despite the large T_g of at least 370 °C, suggesting that PIMs form glasses atypically far from equilibrium due to their rigid and contorted chain structure.

In typical studies of physical aging in polymers, the aging clock is reset by heating a film above its T_g.[13] The absence of an accessible glass transition in PIM-1 prevents use of this strategy. Immersion in alcohols, which causes PIM-1 to visibly swell and increases its post-drying permeability to that of an un-aged film[9], is thus considered a rejuvenation technique analogous to annealing above T_g.

The glass transition and physical aging are complex phenomena constituting an active area of research. In porous polymers, one of the most important properties affected by aging is permeability. Rather than discussing porosity, typical aging studies frame observations in terms of the 'free volume' accessible for molecular motion of polymer chains or permeant molecules. The relationship between permeability P and free volume v_f is exponential:

$$P = DS = Ae^{-B/v_f}$$

with A and B representing empirical constants for a given gas molecule.[17] Changes in the total amount of free volume have a large impact on the diffusivity D with minimal effect on the solubility S[13]. However, due to the multi-wall interactions mentioned above, solubility is enhanced by a match between the *size* of free volume elements and gas molecules.

The porosity in microporous polymers—as measured by positron annihilation or X-ray scattering experiments, in which very small probes interact with individual electrons—is equivalent to the difference between the specific volume occupied by the bulk polymer and the specific volume occupied by its atoms. This specific *unoccupied* volume, or pore volume fraction, is difficult to calculate accurately for polymers, but a number of group contribution methods have been explored.[17]

Although free volume is clearly related to unoccupied volume, precise definitions vary depending on context.[18] When the concept of free volume is invoked to explain dynamic phenomena or mechanical properties, it is sometimes taken to be the unoccupied volume *in excess* of that which would remain at equilibrium, maximum packing, or 0 K.[18, 19] Fractional free volume calculated using the Bondi group-contribution method uses the van der Waals volume multiplied by a universal factor of 1.3[20], implying that free volume is proportionally smaller than unoccupied volume (porosity). A similar method with variable coefficients, empirically determined for specified gases and chemical groups, yields improved permeability predictions using Equation 1; the majority of these coefficients are also larger than unity.[17]

Porosity and free volume in PIMs are thus closely related but not precisely equivalent. During physical aging, fractional free volume and pore volume fraction clearly both decrease. However, the proportionality constant between the two may be specific to the polymer and, in the case of permeability, the probe gas molecule. In this work only changes in porosity are measured and discussed, but it can be inferred that free volume changes in a qualitatively similar manner.

For several polymers, faster aging in thinner films has been reported.[13] This increase in aging rate is not accounted for by the extent of T_g reduction in thinner films. However, diffusion of free volume elements toward the surface has been suggested as a mechanism of aging, and such diffusion would likely occur more quickly in thinner films.[13, 21] A study of PIM-1 by depth-resolved PALS[22] showed that in films with thickness less than 1 μm aging is nearly complete within 3 months, whereas in thicker films aging continues much longer. The results were consistent with a model of free volume diffusion. In addition to this thickness effect, aging generally occurs more rapidly when films are held at higher temperatures.[23]

Given the dependence of free volume on these variables, if a PIM scattering feature is hypothesized to arise from porosity—closely related to free volume—investigating its variation with changes in time, aging temperature, and film thickness is a sound test. Comparison with simulated scattering patterns from molecular dynamics simulations of varying densities is another useful check. Simulations of PIMs at different densities have also recently proven useful in understanding the effect of density on adsorption behavior.[24]

Understanding PIM scattering features could also facilitate a valuable direct comparison of performance metrics such as permeability with structural information as a function of sample history. Scattering methods are both widely available and easily applied to film samples, and more relevant to gas separation applications than the powders used in gas adsorption studies due to slow kinetics in films.

Experimental

Film preparation and aging

The synthesis of PIM-1[25], TA-PIM-1 (thioamide-PIM-1)[26], and some variant linear PIMs[27] discussed in ESI has been described elsewhere. PIM chemical structures are illustrated in Figure 1. PIM-1 films were cast from solution in chloroform using leveled borosilicate glass petri dishes as a substrate; TA-PIM-1 films were cast from solution in tetrahydrofuran. During casting, solutions were placed in a desiccator containing fresh desiccant to minimize the presence of water vapor. The valve of the desiccator was left open inside a fume hood to allow a slow rate of evaporation at ambient temperature.

During the detailed aging study, PIM-1 films were cast from solution to thicknesses of approximately 60, 100, and 240 μm, as described above. Films of a given thickness, though aged under conditions, were always cut from the same film to clearly distinguish the effect of thermal history from any preparation artifact. Each film was immersed in ethanol for 30 hours and then placed in a vacuum oven at one of three temperatures: 30 °C, 75 °C, or 125 °C. Films were aged at these temperatures for 25 hours, although the two higher-temperature ovens required several hours to reach the target temperatures. The first series of SAXS patterns, labeled "1 day", was then collected. WAXS patterns labeled "1 day" were collected for a subset of samples the following day.

Samples were then returned to storage under one of three conditions: a vacuum oven at 75 °C, a vacuum oven at 125 °C, or an evacuated Desi-Vac container (VWR) containing indicating desiccant. The third condition is labeled "RT" (room temperature) in data reported below; samples initially treated at all three temperatures were included in this set. After aging for 13 days, a second series of SAXS patterns was collected. A second series of WAXS patterns was collected the following day. All SAXS and WAXS patterns were collected while samples were at room temperature in between aging stages.

X-ray scattering measurements

Small-angle X-ray scattering (SAXS) patterns were collected under vacuum using a Molecular Metrology instrument with pinhole-collimated Cu-Kα radiation (λ = 1.54 Å), a multiwire area detector, and a sample-to-detector distance of either 1.5 m or 0.5 m. In combined SAXS-WAXS patterns collected during the aging study, SAXS patterns were collected in the 0.5-m configuration. A silver behenate standard was used for wavevector calibration. Isotropic two-dimensional patterns were azimuthally averaged and backgrounds were subtracted. A flat-field correction was used to compensate for variation in sensitivity across the detector, calibrated using isotropic radiation from a radioactive ^{55}Fe sample. A glassy carbon standard was used to determine a vertical scaling factor to place data on an absolute scale.[28]

WAXS patterns were collected in transmission geometry using a Rigaku DMAX-RAPID instrument with Cu-Kα radiation (λ = 1.54 Å) collimated using a 0.3-mm pinhole aperture and an image-plate detector. Isotropic two-dimensional patterns were azimuthally averaged into one-dimensional profiles of intensity $I(q)$ vs. scattering wavevector $q = 4\pi(\sin\theta)/\lambda$. Backgrounds were subtracted from all patterns using the transmission measured with the SAXS instrument on the same sample.

WAXS measurements were not inherently calibrated on an absolute-intensity scale. However, there was sufficient overlap in wavevector range between WAXS patterns and SAXS patterns to vertically scale the WAXS data, producing continuous patterns spanning $0.02 < q < 3$ Å^{-1}. Merged patterns are reported in this work with separate SAXS and WAXS patterns shown in Supporting Information, illustrating the good agreement in shape between SAXS and WAXS.

USAXS patterns were collected at beamline 32-ID[29, 30] of the Advanced Photon Source using a Bonse-Hart camera with slit collimation and an incident energy of 12 keV (λ = 1 Å). Backgrounds were subtracted and patterns were desmeared using Irena tools[31] for the application Igor. In combined USAXS/SAXS/WAXS patterns, SAXS and WAXS patterns were scaled to match USAXS intensities.

Molecular dynamics simulations and simulated scattering

Simulations of PIM-1 and characterization of simulated structures were performed using a method developed by Larsen, *et al.*[12, 32] To model PIM-1, chains were grown at a low density (0.07 g/cm^3) and then compressed using a 21-step scheme to a realistic density (~1 g/cm^3) using LAMMPS[33] with bonded parameters from GAFF[34], non-bonded parameters from TraPPE[35], and charges from *ab initio* calculations with Gaussian 03[36] and RESP[37], as given in ref[12]. These cubic boxes were ~81 Å in length at 1 bar, a significantly larger size than usual because the wavevector range of simulated scattering patterns is limited by the box size L: $q_{min} = 2\pi/(L/2)$. Details of box sizes and densities throughout the compression scheme are given in ESI.

Simulated X-ray scattering patterns were computed using ISAACS software.[38] A geometrical measure of surface area was calculated using a Monte Carlo integration procedure developed by Düren, *et al.*[39] Pore volume fraction (called 'fractional free volume' in related works[12, 32, 40]) and pore size distribution (PSD) were calculated using a different Monte Carlo integration method described by Gelb and Gubbins.[41]

Results and discussion

Interpretation and analysis of PIM scattering features

Scattering patterns from PIM-1 films include three principal features: power-law ($I \propto q^{-3}$) scattering at low q, a broad SAXS/WAXS feature with a maximum near 0.27 Å^{-1}, and a group of weak peaks at 0.9 Å^{-1} and larger wavevectors. Figure 2 illustrates these in comparison with a pattern from atactic polystyrene (aPS), a typical nonporous amorphous polymer exhibiting high-q amorphous halos, negligible small-angle

scattering, and a power-law upturn at low q with onset near 0.1 Å^{-1}.

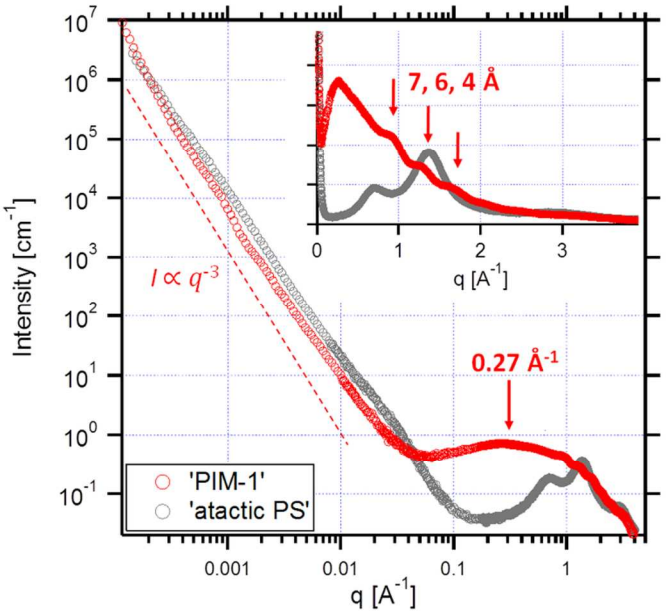

Figure 2. Broad q range X-ray scattering data for a PIM-1 film (red), shown in comparison with atactic polystyrene (compression-molded film; grey). Data includes combined USAXS, SAXS and WAXS patterns, with SAXS and WAXS data scaled to overlap with USAXS data. Inset: the same data plotted on a linear-linear scale.

In PIMs the principal source of scattering contrast is between polymer and empty space (unoccupied volume, or porosity). Because pore sizes are defined by distances between neighboring chain segments, one might expect to observe amorphous halos shifted to slightly lower q compared with nonporous polymers, indicating larger intersegmental distances. However, the patterns observed are much more complex. PIM-1 films exhibit strong scattering throughout the SAXS range. This broad feature is centered at 0.27 Å^{-1}, and the corresponding Bragg spacing of 23 Å is much larger than any pore size measured in PIM-1 (< 10 Å by simulations, PALS, and gas sorption). The asymmetry of this peak on a linear scale (Figure 2, inset) also contrasts with typical amorphous halos.

Weak high-q features. Superimposed on this broad SAXS/WAXS feature are at least three peaks, and although their wavevectors are comparable to those of typical amorphous halos, their intensities are much weaker. Our previous work examining partial simulated structure factors[42] indicated that correlations among atoms in rigid segments predominantly give rise to the high-q edge of the broad SAXS/WAXS feature, while correlations among atoms in spirocenters contribute mainly to the weak high-q features. This suggests that high-q features represent characteristic distances between spirocenters on different chains, a subtle distinction from the usual interpretation of amorphous halos as arising from intersegmental distances. Scattering patterns from PIMs of varied chemistries discussed in ESI also support this interpretation. There is also no evidence of trimodal pore size distributions from any characterization technique, including simulations that reproduce these scattering features. Altogether, this suggests that the weak high-q scattering features do not provide a direct measurement of either unoccupied volume or pore sizes.

Low-q power-law scattering. Low-q power-law scattering is observed in many amorphous homopolymers. Although the source is not well understood, low-q scattering from PIM-1 does not exhibit a dependence on sample history and falls within the range of intensity and power-law slope observed in other, nonporous polymers, which both suggest that it is not linked with microporosity. We also note that while a specific surface area can be extracted from power-law scattering, using the low-q scattering would yield the surface area of objects orders of magnitude larger than micropores, and if power-law scattering occurs at high q it is obscured by other features. See ESI for scattering patterns and further discussion.

Hypothesis: Broad SAXS/WAXS feature is linked with porosity. The strong small-angle scattering with a maximum at 0.2 to 0.4 Å^{-1} observed here as well as in other PIMs[43] is the most striking difference from nonporous amorphous homopolymer scattering patterns. Scattering arising from porosity is expected to decrease in intensity when porosity is lower, due either to sample history or polymer chemistry.

Effect of high density on simulated scattering patterns. A simulated structure generation process for PIMs[12, 32] including compression under high pressures provided an opportunity to examine the effect of a large change in porosity on PIM scattering. Because the wavevector range of simulated scattering patterns is limited by the box size, larger boxes than typically studied—80 Å in length, compared to 45 Å—were necessary to study scattering in the range of the broad SAXS peak.

Table 1. Surface area and density of PIM-1 boxes during compression and decompression. Error bars represent the standard deviation over 10 boxes; boxes were ~81 Å in length in the final configuration. The sequence of compression and decompression steps is described in greater detail in ESI.

Pressure (bar)	Surface area (m^2/g)[a]	Density (g/cm^3)
1000	385 ± 22	0.997 ± 0.007
30000	0.37 ± 0.26	1.463 ± 0.002
50000	0.02 ± 0.02	1.568 ± 0.002
25000	0.47 ± 0.27	1.441 ± 0.002
5000	64 ± 9	1.167 ± 0.006
500	386 ± 45	0.988 ± 0.011
1	573 ± 36	0.941 ± 0.008

[a] Calculated using a N_2 molecule probe size.

As expected, simulation density increased as pressure increased, virtually eliminating porosity (Table 1). Simulated scattering patterns (Figure 3) exhibited a high intensity below 1 Å^{-1}, although the maximum near 0.27 Å^{-1} was not reproduced clearly. The patterns shown are the average of 10 independently generated boxes; scattering patterns from each included a number of extra low-q peaks that appeared at different wavevectors in each box, producing large error bars at low q.

Despite the imperfect agreement with experimental data, the association between porosity and the broad scattering feature is clear: the strong scattering below 1 Å^{-1} was reproduced by simulations with no pores larger than 10-12 Å in diameter, and this scattering diminished as the porosity of the simulated structures decreased.

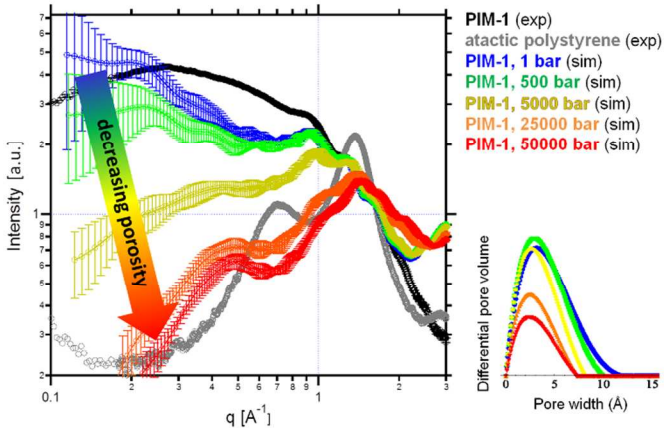

Figure 3. Effect of increased density on simulated scattering patterns and pore size distributions from PIM-1. Error bars represent the standard deviation over 10 boxes (≈ 81 Å in length at 1 bar). While the relative scaling between simulated and experimental data is arbitrary, all simulated scattering patterns are on the same intensity scale, and both experimental patterns are on the same scale.

The spectrum of experimental PIM-1 scattering patterns arising from varied aging conditions explored later in this work (Figures 8 and ESI-19, top) correspond in shape to simulated patterns mainly between 1 bar and 500 bar (0.94 to 0.99 g/cm^3), perhaps up to 5000 bar (1.17 g/cm^3). This range of densities is physically reasonable for a glass under ambient conditions, in contrast to the densities of up to 1.57 g/cm^3 at higher simulated pressures. However, these artificially high densities dramatically illustrate the connection between density and the broad scattering feature associated with PIM porosity.

Effect of sample history and chemistry on scattering intensity. Soaking aged PIM films in alcohols has been shown to reverse the effect of aging, as quantified by permeability measurements.[9] Figure 4 illustrates the effect of this 'rejuvenation' procedure on scattering patterns from PIM-1 and thioamide-PIM-1 (TA-PIM-1) films: recently swollen films have larger scattering intensity, which strongly supports the association of this scattering feature with porosity. In addition, scattering intensity is larger in PIM-1 than in TA-PIM-1, which is a post-synthesis modification with lower porosity and permeability than its parent PIM-1 polymer.[26] In both PIM-1 and TA-PIM-1 the scattered intensity is higher for methanol-treated than for ethanol-treated films, suggesting that methanol may be more effective at reversing physical aging.

Recommendations for qualitative interpretation of PIM scattering data. Although previous authors have interpreted wide-angle scattering peaks from PIM powders as a measurement of pore sizes[44, 45], previous work[42] as well as the insensitivity of high-*q* features to sample history suggests a different interpretation. The broad SAXS/WAXS feature at 0.2 to 0.4 Å^{-1} responds strongly to simulated changes in density as well as changes in sample history that also influence permeability. Qualitatively, scattering can be used to compare films of the same polymer with different sample histories (aging, swelling), or to compare films of two different PIMs

Figure 4. Effect of sample history on absolute-intensity SAXS/WAXS patterns from PIM-1 (left) and TA-PIM-1 (right) films. Green patterns are from solution-cast films aged for 2 years (PIM-1) or 6 months (TA-PIM-1) before scattering experiments. Larger scattering intensities are observed from identical films soaked in methanol (red) or ethanol (blue) for 24 hours prior to scattering measurements. (SAXS measurements were performed under vacuum, removing residual alcohol molecules; liquid-filled pores would produce lower-intensity scattering patterns due to reduced electron-density contrast.)

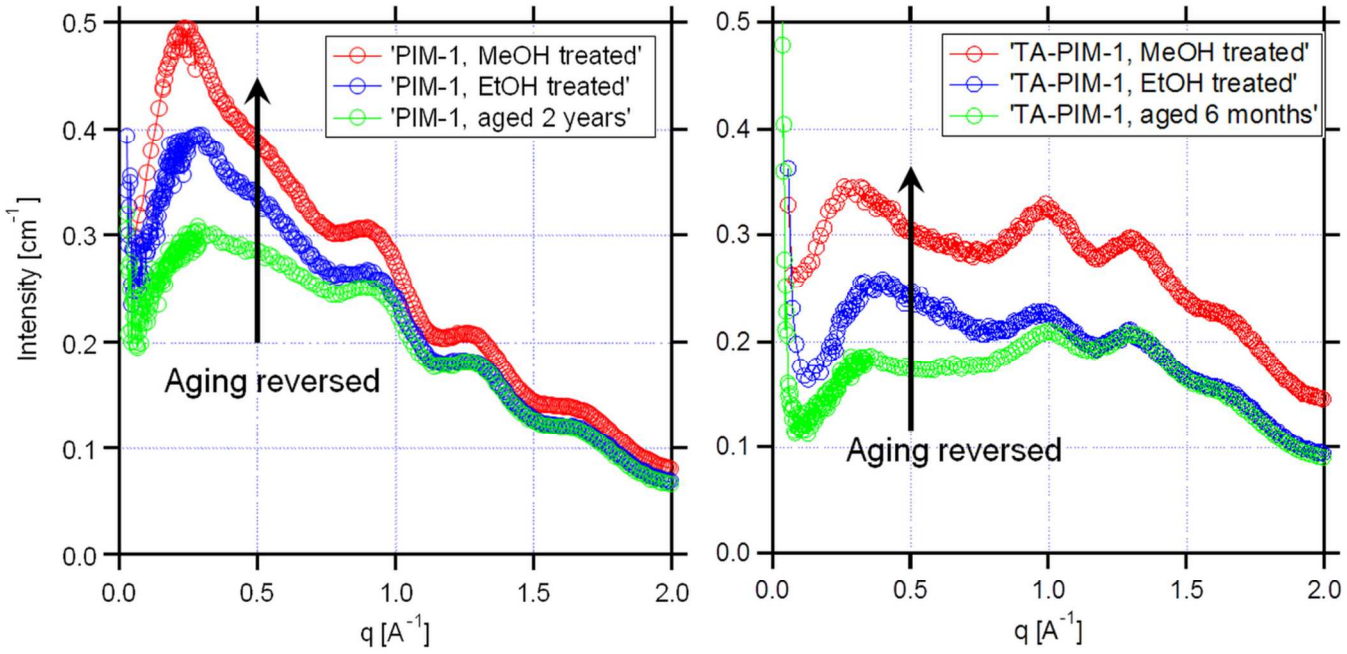

with the same sample history. In both cases, larger absolute scattering intensity corresponds with larger porosity.

SEMI-QUANTITATIVE ANALYSIS OF PIM SCATTERING DATA. Modeling efforts to reproduce the broad SAXS-WAXS feature by treating PIMs as a two-phase system—polymer and unoccupied volume—are detailed in ESI. Parameters derived from both a polydisperse hard-sphere model and the nonparticulate, bicontinuous Teubner-Strey model are physically reasonable enough to support the association of this feature with porosity. However, neither is satisfactory for quantitative comparison of one scattering pattern with another.

In the following aging study, we take the scattering invariant Q as a model-independent indicator of changes in pore volume fraction. The invariant quantifies the net scattering power of a sample. It is determined only by the mean square fluctuation in scattering length density and is not sensitive ("invariant") to the spatial distribution of phases within it.[46] Integration of $I(q)$ including a q^2 factor is appropriate for scattering patterns from isotropic materials which have been azimuthally integrated:

$$Q = \frac{1}{2\pi^2}\int_0^\infty q^2 I(q)dq = V(\Delta\rho)^2\varphi_1\varphi_2$$

where V is the sample volume, $\Delta\rho$ is the difference in scattering length density between the two phases, and φ_1 and φ_2 are respectively the volume fractions of polymer and unoccupied volume. The invariant, proportional to $\varphi_2(1-\varphi_2)$, is a more sensitive measurement of changes in pore volume fraction near $\varphi_2 = 0.25$ (a reasonable value for PIM-1) than film thickness t, related to φ_2 by

$$\frac{t}{t_{\varphi_2=0}} = (1-\varphi_2)^{-1/3}$$

For example, if φ_2 increases from 0.2 to 0.3, the invariant increases by 31% while film thickness increases by only 4.6% (Figure 5).

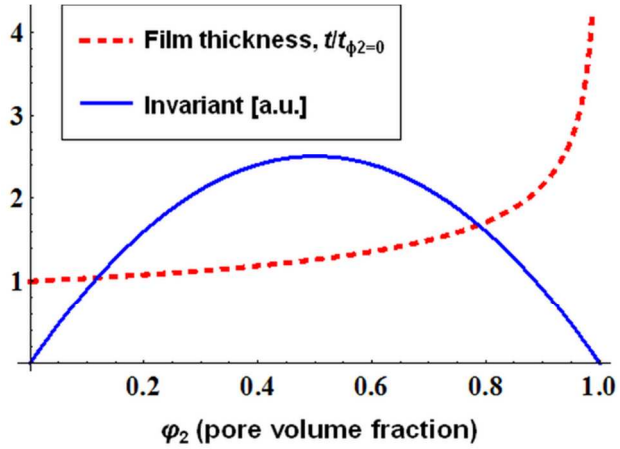

Figure 5. Relative film thickness (red, dashed) and the scattering invariant (blue, solid) plotted as a function of pore volume fraction φ_2.

In practice, $I(q)$ is never measured over an infinite q range. For PIMs, it might be preferable to choose the integration limits q_{min} and q_{max} within an even narrower range than most of the patterns shown in order to reduce contributions that are not related to porosity, such as the low-q upturn or weak high-q features. In addition to calculation of the invariant, the peak maximum also provides some indication of changes in pore sizes, although it may also be sensitive to large changes in pore volume fraction.

Effect of physical aging on PIM-1 scattering patterns

Structural change during physical aging includes an increase in density and a corresponding decrease in free volume. Because porosity in PIMs is correlated with free volume, and the broad SAXS/WAXS feature is closely related to porosity, changes in scattering patterns are predicted to accompany physical aging in PIMs.

In most physical aging studies, the 'clock' is set to zero by heating the film above T_g. PIMs exhibit no glass transition temperature below their decomposition temperature; instead, immersing films in an alcohol such as methanol or ethanol is a widely used rejuvenation technique. Films swell while immersed in alcohols, and after removal and evaporation of residual alcohol they exhibit higher gas permeability, at least equal to that of freshly cast films[9]. Figure 4 illustrates the first test of the effect of aging on PIM scattering patterns: rejuvenated films exhibit larger scattering intensity than films aged for a long period of time.

In addition to time, two additional variables are known to influence aging behavior: film thickness and aging temperature. If a film is held at a higher temperature—provided it is still below T_g—more thermal energy is available for the dynamic process that constitutes aging. Thinner films have been observed to age at a faster rate, as quantified by permeability measurements; the mechanism invoked to explain this is diffusion of free volume elements toward the film surface, which would occur more quickly in thinner films[13, 22, 23].

ACCELERATED AGING AT HIGHER TEMPERATURES. Scattering patterns from films of the same thickness aged for 1 day exhibited lower intensity after aging at higher temperatures (Figure 6). The strong association of this scattering feature with porosity implies that films stored at higher temperatures aged more quickly. Similar changes were observed in films of other thicknesses, but large differences were not observed between 1 and 14 days of aging.

All films stored for two weeks at 125 °C exhibited a change in color from translucent bright yellow to a slightly more opaque yellow-orange, suggesting that some chemical reaction occurred. Although the color change was not apparent after only one day at 125 °C, patterns from all films exposed to 125 °C for two weeks should be interpreted with some caution. However, samples treated at 125 °C for several months were still fully soluble in chloroform, suggesting that extensive cross-linking, such as between pairs of nitrile groups, did not occur.

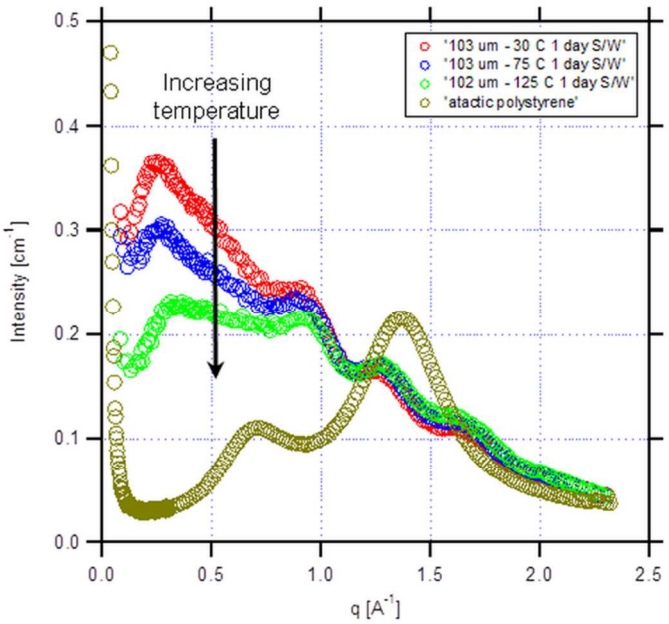

Figure 6. Combined SAXS/WAXS patterns from three PIM-1 films ~100 μm in thickness aged for one day at 30 °C (red), 75 °C (blue), or 125 °C (green). A pattern from atactic polystyrene (compression-molded and aged for several years; brown) is included for comparison: although PIM SAXS intensity decreases during aging at higher temperatures, it is still relatively large.

Figure 7. Combined SAXS/WAXS patterns from PIM-1 films aged for one day at 30 °C (left), 75 °C (middle), or 125 °C (right) with thicknesses of ~240 μm (red), ~100 μm (blue), and ~60 μm (green).

ACCELERATED AGING IN THINNER FILMS. Figure 7 compares SAXS patterns from PIM-1 films ~60, ~100 and ~240 μm in thickness, aged for one day at 30 °C (left), 75 °C (middle), or 125 °C (right). At all temperatures, 100-μm films exhibited slightly lower scattering intensity than 240-μm films, and 60-μm films exhibited significantly lower intensity.

EFFECT OF AGING ON THE SCATTERING INVARIANT AND PEAK POSITION. While most aging studies naturally analyze measured quantities as a function of time, the small differences observed between scattering patterns from a given film measured after one day and after two weeks indicate that the largest structural changes occurred during the first day. The separate laboratory SAXS and WAXS instruments used in this study, each requiring an hour or more of data collection for the thinnest samples, are not suitable for resolving time scales shorter than one day. However, the variety in scattering patterns from samples of different thicknesses aged for one day under different conditions (Figure 8, top) demonstrates that a wide spectrum of glassy states was measured by manipulating film thickness and aging temperature. *If* it is hypothesized that a single film moves through this same continuum of glassy states during aging, then this set of data serves as the basis for a discussion of possible structural changes during aging of PIMs.

In Figure 8 (top), the patterns shown in Figure 7 are combined into one plot with a log scale in q to highlight the SAXS feature associated with porosity. This reveals that the wavevector of the peak maximum is relatively constant across a range of the largest scattering intensities; however, at lower scattering intensities it moves to larger wavevectors. Qualitatively, these regimes can be interpreted respectively as diffusion of pores—a reduction in pore volume fraction with

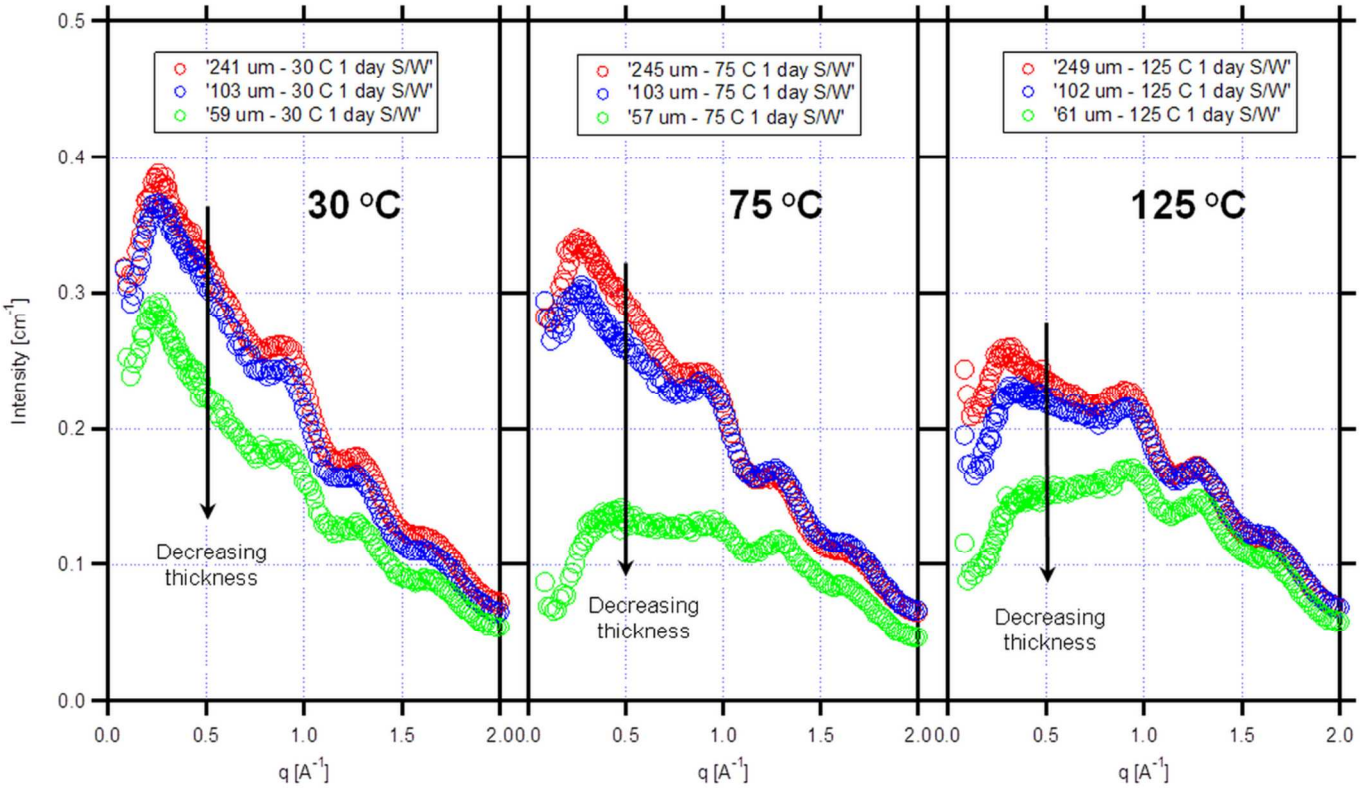

little change in the shape of the pore size distribution—and 'shrinking' of pores. Pore shrinking could occur either by preferential loss of the largest pores or by a decrease in the size of individual pores.

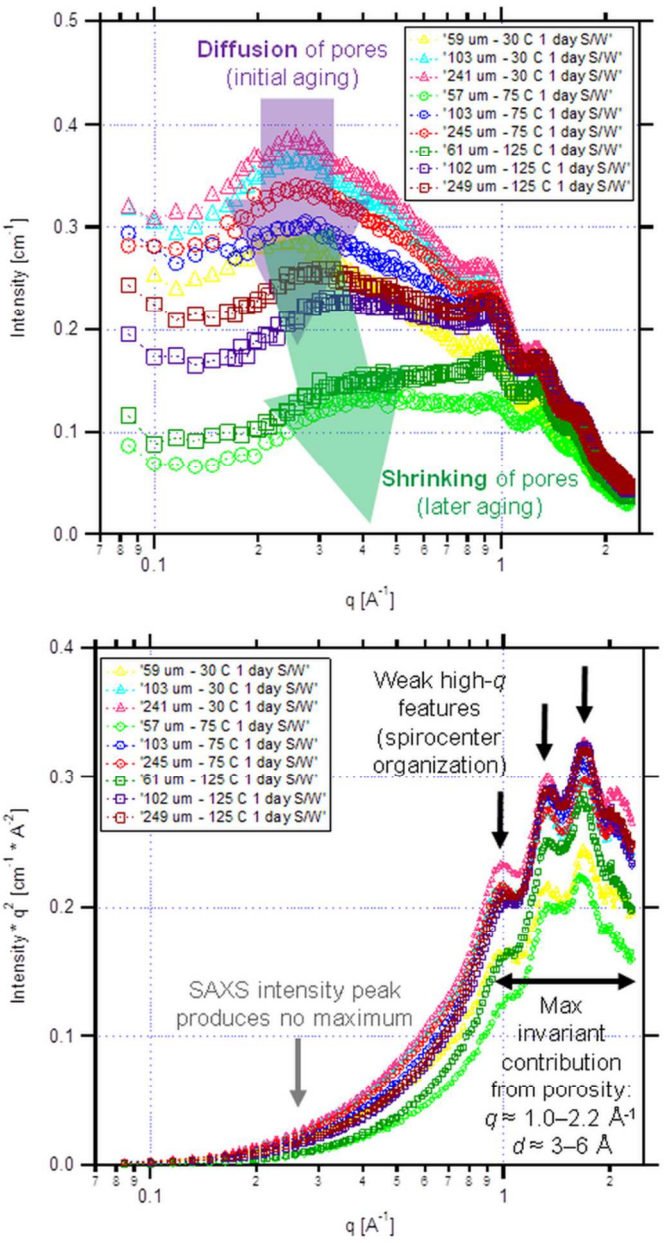

Figure 8. SAXS/WAXS patterns from PIM-1 films aged for one day, shown in Figure 7, are combined into one plot (top). The integrand of the scattering invariant, q^2I, is also plotted with the same horizontal axis (bottom). There was little change in the corresponding scattering patterns measured again after two weeks (ESI).

To examine this aging behavior semi-quantitatively, the scattering invariant was used as an indication of pore volume fraction and the maximum wavevector of the broad SAXS feature as an indication of pore sizes. In the lower half of Figure 8, the integrand of the scattering invariant is plotted versus q to illustrate the contributions from different scattering features to the total invariant. There is no maximum in q^2I corresponding to the SAXS maximum, although the weak high-q features related to the organization of spirocenters are evident. The maximum contribution to the invariant arising from porosity is obscured by these but lies somewhere in the range of 1.0 to 2.2 Å^{-1}. The corresponding real-space size scale of 3 to 6 Å is comparable to pore sizes measured by other techniques.

Figure 9 displays the partial scattering invariant for each scattering pattern collected—using integration limits of q = 0.1 to 0.5 Å^{-1}—as a function of sample thickness. These integration limits were selected to exclude parts of the scattering pattern dominated by the low-q upturn, or by high-q scattering that arises in part from local segmental order and persists even when porosity is largely eliminated under high simulated pressure (Figure 3). This integration range may include some non-porous scattering and exclude some high-q scattering from small pores, but the values reported in Figure 9 are comparable to one another.

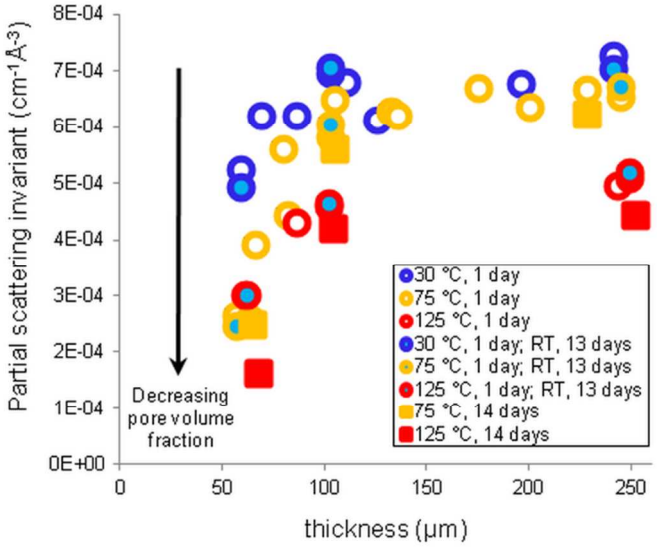

Figure 9. Partial scattering invariant—using integration limits of q = 0.1 to 0.5 Å^{-1}—calculated from PIM-1 SAXS patterns for a variety of thicknesses and thermal histories. Open circles represent films aged for one day at 30 °C (blue), 75 °C (yellow), or 125 °C (red). Circles of the same color scheme filled with blue correspond to films subsequently stored for 13 days at ambient temperature. Filled squares represent films stored at elevated temperatures for two weeks. Data from some films whose patterns are not shown in Figures 4 through 9 is also included; these patterns (SAXS only) are shown in ESI.

The clearest general trend in Figure 9 is the lower pore volume fraction in films thinner than ~100 μm, evident for all thermal histories. Differences in pore volume fraction between 100- and 240-μm films aged near room temperature are negligible, but 100-μm films aged somewhat faster at 75 °C. In most cases, there was little difference between patterns collected after one day of aging (open circles) and those collected after 13 additional days of aging at room temperature (filled circles) or a higher temperature (filled squares).

At each thickness, aging at higher temperatures during the first day resulted in lower pore volume fractions (Figure 9), with only a small additional decrease during the next two weeks (ESI). The exception to this was that 60-µm films aged to a greater extent during the first day at 75 °C than at 125 °C.

Figure 10 displays the peak positions for all patterns collected as a function of sample thickness. Although the position of this scattering maximum is not a direct indication of the size of pores, it may cautiously be interpreted as a relative indication of differences in the sizes of pores. The large error bars on the peak position in Figure 10 as the peak moves to larger wavevectors occur because it begins to overlap with the weak high-q features (Figure 8, top). With more quantitative modeling to separate these contributions to the scattering pattern, these error bars could be reduced. However, a clear lower bound on the peak position (upper bound on pore size) can always be established.

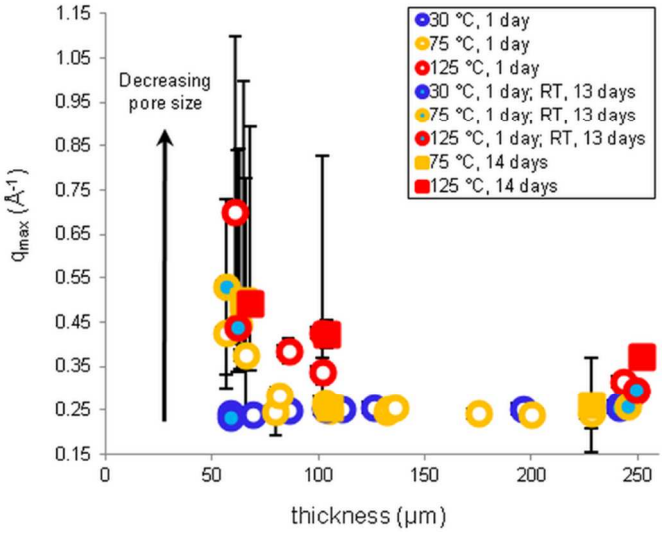

Figure 10. Position of the broad maximum in PIM-1 SAXS patterns for a variety of thicknesses and thermal histories. Error bars on q_{max} correspond to the error arising from a least-squares fit of a Gaussian peak, multiplied by four to allow for the somewhat arbitrary selection of a restricted q range near the maximum for peak fitting. As the SAXS maximum moves to higher q, error bars are very large due to the nearby WAXS peaks. Wavevector maxima from some films whose patterns are not shown in above figures are also included; these patterns (SAXS only) are shown in ESI.

The small differences between patterns collected after one day and two weeks of aging, along with the remaining greater pore volume fraction in thicker films, suggest that the thinnest films may be able to age more extensively at a given temperature: 60-µm films exhibited lower pore volume fractions than thicker films for each thermal history. However, when stored at room temperature, peak positions in 60-µm SAXS patterns were very similar to peak positions from thicker films aged at either room temperature or 125 °C (Figure 10). When aged at 75 °C, 60-µm films exhibited a maximum at higher q, which may indicate smaller pores. Taken together, these observations suggest that aging at different temperatures—and perhaps at different thicknesses—may occur by fundamentally different mechanisms. Figure 11 directly compares the peak maxima and partial scattering invariants for all patterns.

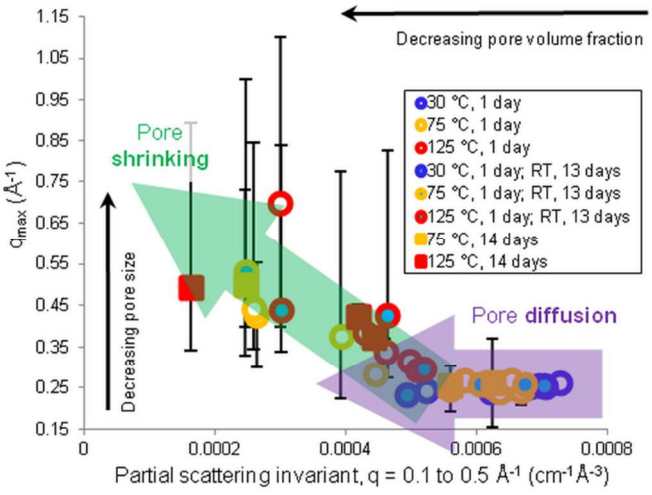

Figure 11. The wavevector of the SAXS peak maximum (Figure 10, vertical axis) plotted against the partial scattering invariant (Figure 9, vertical axis). Film thicknesses are not indicated in this figure; samples may be regarded as accessing different regions of an aging phase diagram through a combination of varied temperature and film thickness, rather than by tracking a single film as a function of time.

Examining Figure 11, the peak maximum is relatively constant across a range of values of the pore volume fraction. Aging in this regime, highlighted in purple, could correspond to diffusion of free volume elements toward a free surface where they are lost. However, below some critical value of the pore volume fraction, the peak maximum begins to move to higher q as the pore volume fraction decreases. This regime, highlighted in green, could be explained by the shrinking of pores. Changing the upper limit of integration for calculating the invariant to 1.0 or 2.0 Å^{-1} results in plots with this same characteristic shape, except that films exposed to 125 °C deviate from the pattern (ESI). This may suggest that pore shrinking occurs more quickly relative to pore diffusion at elevated temperatures, or that the observed change in color (at 125 °C only) indicated a change in chemistry that altered the usual aging process.

Conclusions

PIMs form microporous films with applications in gas separation and storage, but their performance as membranes is impacted by physical aging. Scattering methods offer a convenient method for studying the structure of PIM films with well-defined sample history; the broad high-q SAXS feature is clearly very sensitive to porosity, although improved scattering models are needed to quantify the size distribution of pores and pore volume fraction.

PIMs also constitute a useful model system for studying changes in intrinsic microporosity, closely related to free volume, during aging. A better understanding of interactions between PIM films and the nonsolvent organic liquids used to rejuvenate them would facilitate comparison with the existing body of work on physical aging in glasses.

Changes in PIM-1 scattering patterns as a function of film thickness and storage temperature consistent with physical aging were observed: storing films at higher temperatures resulted in lower-intensity scattering patterns. Below a threshold of approximately 100 μm, films were able to age more quickly and/or to a greater extent, resulting in lower pore volume fractions than observed in thicker films with equivalent thermal histories. The existence of a threshold value for film thickness dependence of aging behavior—quantified by permeability—has been reported for other polymers[23], but the threshold thickness in PIM-1 is larger by a factor of 2 to 10. A similar investigation of the effect of PIM film thickness on the rate of permeability decrease would confirm the dependence suggested by the scattering data reported here.

Comparing the dependence of pore volume fraction (quantified by the scattering invariant) and pore size (as roughly estimated by the peak maximum) on film thickness and thermal history suggests that more than one mechanism of aging may be possible. To investigate this possibility, the peak position was plotted against the partial invariant, regarding films of different thicknesses and thermal histories as accessing different portions of a PIM aging phase diagram. Points on this plot fell into two distinct regimes: at high volume fractions, the peak position was nearly constant; below a threshold volume fraction, the peak moved to higher q as volume fraction decreased. These two regimes are interpreted respectively as diffusion and shrinking of pores during aging.

We emphasize that the hypothesis of dual aging mechanisms is based on examining a range of glassy states produced by varying film thickness and aging temperature, *not* by measuring a single film over time. Using a synchrotron X-ray source, aging during the first minutes or hours could be investigated. In addition, a plot similar to Figure 11 could be made using pore sizes from PALS and fractional free volume from permeability measurements.

Acknowledgements

Support for this project was provided by the National Science Foundation (DMR-0908781) and EPSRC (EP/G065144/1) through the Materials World Network program, as well as the NSF Polymers Program (DMR-1206571). AGM also acknowledges funding from the NSF Graduate Research Fellowship program (DGE-0750756).

Louise Maynard-Atem, Nhamo Chaukura, and Chris Mason (Manchester) synthesized samples of PIM-1 and TA-PIM-1. Mariolino Carta and Kadhum Msayib (Cardiff) synthesized additional variant PIMs shown in SI. USAXS patterns shown in SI were collected at Beamline 32-ID (now 15ID-D) of the Advanced Photon Source at Argonne National Laboratory (DOE BES DE-AC02-06-CH11357) with the assistance of Jan Ilavsky, who also provided the glassy-carbon standard used for absolute-intensity SAXS calibration.

Many other colleagues have shared useful insights, including Flor Siperstein (Manchester) as well as Lauren Abbott, Kyle Hart, Greg Larsen, Mark Angelone, Ralph Colby, and Scott Milner (Penn State). In particular, John Jansen (Institute on Membrane Technology, NRC of Italy) provided helpful suggestions for the initial design of the aging study.

Notes and references

[a] Department of Materials Science and Engineering, The Pennsylvania State University, University Park, PA 16802. Corresponding email: runt@matse.psu.edu.

[b] School of Chemistry, The University of Manchester, Manchester, M13 9PL, UK.

[c] School of Chemistry, Cardiff University, CF10 3AT, UK.

[†] Present address (AGM): Materials Science and Engineering Division, National Institute of Standards and Technology, Gaithersburg, MD 20899; amanda.mcdermott@nist.gov.

[‡] Present address (NBM): School of Chemistry, University of Edinburgh, Edinburgh, Scotland EH9 3JJ.

Electronic Supplementary Information (ESI) available: (1) Additional experimental scattering data supporting the interpretation of PIM scattering features; (2) A discussion of hard-sphere and Teubner-Strey scattering models applied to PIM scattering patterns; (3) Full SAXS and WAXS patterns, along with partial scattering invariants calculated using alternate integration limits; and (4) Details of molecular dynamics simulations. See DOI: 10.1039/b000000x/

1. P. M. Budd and N. B. McKeown, *Polym. Chem.*, 2010, **1**, 63-68.
2. N. B. McKeown and P. M. Budd, in *Encyclopedia of Membrane Science and Technology*, eds. E. M. V. Koek and V. V. Tarabara, John Wiley and Sons, Inc., 2013, vol. 2, p. 781.
3. A. D. McNaught and A. Wilkinson, eds., *IUPAC Compendium of Chemical Terminology (the "Gold Book")*, Blackwell Scientific Publications, 1997.
4. S. J. Gregg and K. S. W. Sing, *Adsorption, Surface Area and Porosity*, Academic Press Inc., New York, 1982.
5. N. B. McKeown and P. M. Budd, *Macromolecules*, 2010, **43**, 5163-5176.
6. P. M. Budd, N. B. McKeown and D. Fritsch, *Macromolecular Symposia*, 2006, **245-246**, 403-405.
7. P. M. Budd, B. S. Ghanem, S. Makhseed, N. B. McKeown, K. J. Msayib and C. E. Tattershall, *Chemical Communications*, 2004, **2004**, 230-231.
8. J. Rouquerol, D. Avnir, C. W. Fairbridge, D. H. Everett, J. M. Haynes, N. Pernicone, J. D. F. Ramsay, K. S. W. Sing and K. K. Unger, *Pure and Applied Chemistry*, 1994, **66**, 1739.
9. P. M. Budd, N. B. McKeown, B. S. Ghanem, K. J. Msayib, D. Fritsch, L. Starannikova, N. Belov, O. Sanfirova, Y. Yampolskii and V. Shantarovich, *Journal of Membrane Science*, 2008, **325**, 851-860.
10. P. M. Budd, N. B. McKeown and D. Fritsch, *Journal of Materials Chemistry*, 2005, **15**, 1977-1986.
11. C. L. Staiger, S. J. Pas, A. J. Hill and C. J. Cornelius, *Chemistry of Materials*, 2008, **20**, 2606-2608.
12. G. S. Larsen, P. Lin, K. E. Hart and C. M. Colina, *Macromolecules*, 2011, **44**, 6944-6951.
13. Y. Huang and D. R. Paul, *Polymer*, 2004, **45**, 8377-8393.
14. F. Y. Li and T.-S. Chung, *International Journal of Hydrogen Energy*, 2013, **38**, 9786-9793.

15. P. Bernardo, F. Bazzarelli, J. C. Jansen, G. Clarizia, F. Tasselli and C. R. Mason, *Procedia Engineering*, 2012, **44**, 874-876.
16. A. F. Bushell, P. M. Budd, M. P. Attfield, J. T. A. Jones, T. Hasell, A. I. Cooper, P. Bernardo, F. Bazzarelli, G. Clarizia and J. C. Jansen, *Angewandte Chemie International Edition*, 2013, **52**, 1253-1256.
17. J. Y. Park and D. R. Paul, *Journal of Membrane Science*, 1997, **125**, 23-39.
18. A. Bondi, *The Journal of Physical Chemistry*, 1954, **58**, 929-939.
19. P. C. Painter and M. M. Coleman, *Fundamentals of Polymer Science*, CRC Press, 1997.
20. A. Bondi, *Physical properties of molecular crystals, liquids and glasses*, Wiley, New York, 1968.
21. D. R. Paul and L. M. Robeson, *Polymer*, 2008, **49**, 3187-3204.
22. S. Harms, K. Rätzke, F. Faupel, N. Chaukura, P. M. Budd, W. Egger and L. Ravelli, *The Journal of Adhesion*, 2012, **88**, 608-619.
23. Y. Huang and D. R. Paul, *Macromolecules*, 2005, **38**, 10148-10154.
24. K. E. Hart, J. M. Springmeier, N. B. McKeown and C. M. Colina, *Physical Chemistry Chemical Physics*, 2013, **15**, 20161-20169.
25. P. M. Budd, E. S. Elabas, B. S. Ghanem, S. Makhseed, N. B. McKeown, K. J. Msayib, C. E. Tattershall and D. Wang, *Advanced Materials*, 2004, **16**, 456-459.
26. C. R. Mason, L. Maynard-Atem, N. M. Al-Harbi, P. M. Budd, P. Bernardo, F. Bazzarelli, G. Clarizia and J. C. Jansen, *Macromolecules*, 2011, **44**, 6471–6479.
27. M. Carta, K. J. Msayib, P. M. Budd and N. B. McKeown, *Organic letters*, 2008, **10**, 2641-2643.
28. F. Zhang, J. Ilavsky, G. Long, J. Quintana, A. Allen and P. Jemian, *Metallurgical and Materials Transactions A*, 2010, **41**, 1151-1158.
29. J. Ilavsky, P. R. Jemian, A. J. Allen, F. Zhang, L. E. Levine and G. G. Long, *Journal of Applied Crystallography*, 2009, **42**, 469-479.
30. F. Zhang and J. Ilavsky, *Polymer Reviews*, 2010, **50**, 59-90.
31. J. Ilavsky and P. R. Jemian, *Journal of Applied Crystallography*, 2009, **42**, 347-353.
32. G. S. Larsen, P. Lin, F. R. Siperstein and C. M. Colina, *Adsorption*, 2011, **17**, 1-6.
33. S. Plimpton, *Journal of Computational Physics*, 1995, **117**, 1-19.
34. J. Wang, R. M. Wolf, J. W. Caldwell, P. A. Kollman and D. A. Case, *Journal of Computational Chemistry*, 2004, **25**, 1157-1174.
35. C. D. Wick, M. G. Martin and J. I. Siepmann, *The Journal of Physical Chemistry B*, 2000, **104**, 8008-8016.
36. M. J. Frisch, G. W. Trucks, H. B. Schlegel, G. E. Scuseria, M. A. Robb, J. R. Cheeseman, J. A. Montgomery, T. Vreven, K. N. Kudin, J. C. Burant, J. M. Millam, S. S. Iyengar, J. Tomasi, V. Barone, B. Mennucci, M. Cossi, G. Scalmani, N. Rega, G. A. Petersson, H. Nakatsuji, M. Hada, M. Ehara, K. Toyota, R. Fukuda, J. Hasegawa, M. Ishida, T. Nakajima, Y. Honda, O. Kitao, H. Nakai, M. Klene, X. Li, J. E. Knox, H. P. Hratchian, J. B. Cross, V. Bakken, C. Adamo, J. Jaramillo, R. Gomperts, R. E. Stratmann, O. Yazyev, A. J. Austin, R. Cammi, C. Pomelli, J. W. Ochterski, P. Y. Ayala, K. Morokuma, G. A. Voth, P. Salvador, J. J. Dannenberg, V. G. Zakrzewski, S. Dapprich, A. D. Daniels, M. C. Strain, O. Farkas, D. K. Malick, A. D. Rabuck, K. Raghavachari, J. B. Foresman, J. V. Ortiz, Q. Cui, A. G. Baboul, S. Clifford, J. Cioslowski, B. B. Stefanov, G. Liu, A. Liashenko, P. Piskorz, I. Komaromi, R. L. Martin, D. J. Fox, T. Keith, A. Laham, C. Y. Peng, A. Nanayakkara, M. Challacombe, P. M. W. Gill, B. Johnson, W. Chen, M. W. Wong, C. Gonzalez and J. A. Pople, Gaussian, Inc., Wallingford, CT, 2003.
37. J. Wang, W. Wang, P. A. Kollman and D. A. Case, *Journal of Molecular Graphics and Modelling*, 2006, **25**, 247-260.
38. S. Le Roux and V. Petkov, *Journal of Applied Crystallography*, 2010, **43**, 181-185.
39. T. Düren, F. Millange, G. Férey, K. S. Walton and R. Q. Snurr, *The Journal of Physical Chemistry C*, 2007, **111**, 15350-15356.
40. G. S. Larsen, Doctor of Philosophy, The Pennsylvania State University, 2011.
41. L. D. Gelb and K. Gubbins, *Langmuir*, 1999, **15**, 305-308.
42. A. G. McDermott, G. S. Larsen, P. M. Budd, C. M. Colina and J. Runt, *Macromolecules*, 2011, **44**, 14-16.
43. J. Weber, N. Du and M. D. Guiver, *Macromolecules*, 2011, **44**, 1763-1767.
44. N. Du, G. P. Robertson, J. Song, I. Pinnau, S. Thomas and M. D. Guiver, *Macromolecules*, 2008, **41**, 9656-9662.
45. N. Du, G. P. Robertson, J. Song, I. Pinnau and M. D. Guiver, *Macromolecules*, 2009, **42**, 6038-6043.
46. E. Huang, M. F. Toney, W. Volksen, D. Mecerreyes, P. Brock, H. C. Kim, C. J. Hawker, J. L. Hedrick, V. Y. Lee, T. Magbitang, R. D. Miller and L. B. Lurio, *Applied Physics Letters*, 2002, **81**, 2232-2234.